Topological edge modes and phase transitions in a critical fermionic chain with long-range interactions

Wen-Hao Zhong [1,*] Wei-Lin Li,[2,3,*] Yong-Chang Chen [1] and Xue-Jia Yu [1,4,†]

[1]*Department of Physics, Fuzhou University, Fuzhou 350116, Fujian, China*

[2]*Key Laboratory of Atomic and Subatomic Structure and Quantum Control (Ministry of Education), Guangdong Basic Research Center of Excellence for Structure and Fundamental Interactions of Matter, School of Physics, South China Normal University, Guangzhou 510006, China*

[3]*Guangdong Provincial Key Laboratory of Quantum Engineering and Quantum Materials, Guangdong-Hong Kong Joint Laboratory of Quantum Matter, Frontier Research Institute for Physics, South China Normal University, Guangzhou 510006, China*

[4]*Fujian Key Laboratory of Quantum Information and Quantum Optics, College of Physics and Information Engineering, Fuzhou University, Fuzhou, Fujian 350108, China*

(Received 20 March 2024; accepted 8 July 2024; published 8 August 2024)

Long-range interactions can fundamentally alter properties in gapped topological phases such as emergent massive edge modes. However, recent research has shifted attention to topological nontrivial critical points or phases, and it is natural to explore how long-range interactions influence them. In this work, we investigate the topological behavior at the quantum critical point of extended Kitaev chains with long-range interactions, which can be derived from the critical Ising model via the Jordan-Wigner transformation in the short-range limit. Specifically, we analytically find that the critical edge modes at the critical point remain stable against long-range interactions. More importantly, we observe that these critical edge modes remain massless even when long-range interactions become very strong. As a by-product, we numerically find that the critical behavior of the long-range model belongs to the free-Majorana-fermion universality class, which is entirely different from the long-range universality class in the usual long-range spin models. Our work could shed new light on the interplay between long-range interactions (frustrated) and the gapless topological phases of matter.

DOI: 10.1103/PhysRevA.110.022212

I. INTRODUCTION

For the past few decades, our understanding has primarily focused on the universal behavior of systems with short-range (SR) interactions, such as lattice systems with nearest-neighbor couplings [1–4]. In recent years, there has been an investigation into the overall picture of novel phenomena in classical and quantum systems with long-range (LR) interactions [5–7]. Increasing the range of interactions $V \sim 1/r^{\alpha}$ (or, equivalently, reducing the power exponent α) can fundamentally alter the "basic laws" of statistical and condensed-matter physics, including the failure of quantum-classical correspondence [8–10], breakdown of the Mermin-Wagner theorem [11,12], emergence of massive edge modes [13–16], and new LR universality classes [17–24], among others. Moreover, the experimental realization of quantum systems with LR interactions, such as cold atomic gases in cavities [25–27], trapped ions [28,29], and programmable Rydberg quantum simulators [30–33], has spurred significant motivation to explore the novel properties of such systems.

On a different front, the development of topological phases of matter has garnered significant attention in the past few decades, expanding our understanding of quantum matter beyond the Landau paradigm [34–40]. A notable example is topological insulators and superconductors [41,42], in which the bulk is gapped and nontrivial gapless edge modes emerge at the boundary [43–46]. However, recent research revealed that many key features of topological physics, such as topological invariants [47–50], the universal bulk-boundary correspondence in the entanglement spectrum [51,52], and degenerate edge modes [53–69], persist despite nontrivial coupling between the boundary and critical bulk modes. Nevertheless, there are still largely unexplored areas within the field of the interplay between topology and quantum criticality even in the free-fermion system [50,70–78].

Recently, there has been a surge of interest in the LR version of an integrable topological fermionic chain, featuring a LR superconducting pairing or hopping term [79–90], which exhibits exotic properties such as massive edge modes [13–16], anomalous behavior of correlation functions [14,87], and novel bulk-boundary correspondence [91]. Unlike the SR case, the LR fermionic and spin chains are two independent models that cannot be mapped to each other through the Jordan-Wigner transformation. Furthermore, LR power-law interactions are ubiquitous in modern quantum simulation platforms [25,28,30]. Therefore, it is fundamentally important to study LR interacting models both theoretically and experimentally. However, over the past few decades, most research efforts have focused on the stability of edge

*These authors contributed equally to this work.
†Contact author: xuejiayu@fzu.edu.cn

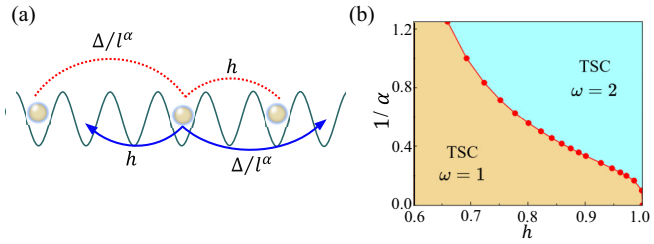

FIG. 1. (a) A schematic representation of the LR interacting fermionic chain is presented. The brown ball denotes the fermion, while the blue line with arrows (red dashed line) represents the LR and next-nearest-neighbor hopping (pairing) term. (b) The global phase diagram illustrates the extended Kitaev chain with LR interactions as a function of the LR power exponent α and the driven parameter h. The phase diagram delineates the topological superconducting phases with winding number ω, denoted as the TSC $\omega = 1$ phase (brown region) and the TSC $\omega = 2$ phase (light blue region). Red points mark the critical points h_c^* corresponding to different α, and the red line forms the critical line between the two phases.

modes in gapped topological phases with LR interactions [13–16,92]. For gapless topological phases, such as topologically nontrivial quantum critical points (QCPs), how the critical edge modes remain stable against LR interactions remains unclear. Moreover, can LR interactions induce a crossover of the critical edge modes from massless to massive, similar to the effects observed in LR interacting gapped topological phases?

To answer the questions outlined above, in this work, we investigate the topological behavior at the QCPs in extended Kitaev chains with LR interactions, which can be derived from the cluster Ising model via the Jordan-Wigner transformation in the SR limit. Specifically, through exact analytical calculations, we find edge modes at the critical point between distinct topological superconducting (TSC) phases that remain stable under LR interactions. Furthermore, we observe that the edge modes remain massless even when LR interactions become very strong, a scenario entirely different from the gapped topological phases with LR interactions. As a by-product, we determine the critical exponent of the LR interacting model that is always consistent with the universality class of the SR one (free Majorana fermion) through finite-size scaling.

This paper is organized as follows: Sec. II introduces the lattice model of the extended Kitaev chain with LR interactions. Section III presents the global phase diagram of the model, finite-size scaling for fidelity susceptibility, and edge modes at the critical points with LR interactions. The conclusion is provided in Sec. IV. Additional data for the analytical and numerical calculations are included in the Appendixes.

II. MODEL AND METHOD

A. Extended Kitaev chain with long-range interactions

In this work, we investigate the behavior of LR interacting fermionic particles on a lattice of length L [see Fig. 1(a)]. The model $H_{\rm LR}$ is described by the following Hamiltonian:

$$H_{\rm LR} = -\Delta \sum_{j=1}^{L} \sum_{l=1}^{L-1} d_l^{-\alpha} (c_j^\dagger c_{j+l} + c_j^\dagger c_{j+l}^\dagger + \text{H.c.}) - h \sum_{j=1}^{L-2} (c_j^\dagger c_{j+2} + c_j^\dagger c_{j+2}^\dagger + \text{H.c.}) - \sum_{j=1}^{L} \mu_j \left(c_j^\dagger c_j - \frac{1}{2} \right). \tag{1}$$

Here, $c_j^\dagger$ (c_j) represents the fermionic creation (annihilation) operator at site j. The parameter h denotes the strength of the next-nearest-neighbor fermion p-wave pairing and hopping amplitude. For a periodic chain, we define $d_l = l$ ($d_l = L - l$) if $l < L/2$ ($l > L/2$) and choose antiperiodic boundary conditions. For an open chain, we define $d_l = l$ and omit terms involving $c_{j>L}$. In this work, we set $\Delta = 1$ as the energy unit, and the chemical potential term $\mu_j = 0$ in the main text. The influence of a uniform and random chemical potential μ_j is discussed in Appendix F.

The Hamiltonian (1) in the SR limit can be derived from the cluster Ising model through the Jordan-Wigner transformation. The latter is an extension of the SR Ising model, exhibiting gapped spontaneous symmetry breaking (SSB) and a cluster symmetry-protected topological (SPT) phase for $h < 1.0$ and $h > 1.0$, respectively, separated by a topologically nontrivial critical point (symmetry-enriched quantum criticality) at $h = 1.0$ [47,48,62,70,93–96]. Upon the Jordan-Wigner transformation, the SSB and SPT phases map to the TSC phase with winding numbers of 1 and 2, respectively. The phase transition between them is characterized by topologically protected Dirac cones [50].

However, with LR interactions, the Hamiltonian (1) is no longer connected to the LR interacting cluster Ising model by a Jordan-Wigner transformation, indicating that their respective phase diagrams may differ. Fortunately, unlike the LR cluster Ising model, Eq. (1) remains exactly solvable, enabling analytical solutions at any finite α. In the following, we explore the topological behavior at the QCPs of the LR fermionic model by examining its winding number and fidelity susceptibility for the periodic chain, as well as the energy spectrum and the critical edge modes for the open one.

III. PHASE DIAGRAM AND TOPOLOGICAL BEHAVIOR

A. Quantum phase diagram

Thanks to the integrability of the model, Eq. (1) can be transformed into momentum space using Fourier transformation:

$$H_{\rm LR} = \sum_k [i y_k (c_k c_{-k} + c_k^\dagger c_{-k}^\dagger) + z_k (c_k^\dagger c_k + c_{-k}^\dagger c_{-k} - 1)]. \tag{2}$$

Here, the wave vector k belongs to $\pm\{2n-1\}\pi/L, n = 1, 2, \ldots, L/2$, and $y_k = [-h \sin(2k) - \Delta f_\alpha(k)]$, and $z_k = [-h \cos(2k) - \Delta g_\alpha(k)]$, with $f_\alpha(k) = \sum_l \sin(kl)/d_l^\alpha$ and $g_\alpha(k) = \sum_l \cos(kl)/d_l^\alpha$. The Hamiltonian is already in a small Hilbert space and can be easily diagonalized by the Bogoliubov transformation (see Appendix A for the details of analytical calculations), and the ground state is given by

$|G\rangle = \prod_{k>0}[\cos(\frac{\theta_k}{2}) + i\sin(\frac{\theta_k}{2})c_k^\dagger c_{-k}^\dagger]|\text{Vac}\rangle$ ($|\text{Vac}\rangle$ is the vacuum state of c fermions).

Before delving into the details of the analytical results, let us summarize our main findings and outline the global quantum phase diagram of the model in Eq. (1). The schematic phase diagram is provided in Fig. 1(b). As α approaches infinity, the model can be derived from the cluster Ising model via Jordan-Wigner duality, and the TSC phases transform to SSB or SPT phases, depending on whether the winding number $\omega = 1$ (brown region) or 2 (light blue region). More importantly, the phase transition between them exhibits a topologically protected Dirac cone with a critical edge mode on an open boundary. When α is finite, we observe that both TSC phases with different winding numbers are stable against LR interactions. Red points mark the critical points corresponding to different α, and the red line forms the critical line between the two phases. Whether LR interactions influence the physics of critical edge modes is the crucial issue in this work, and we will address it in the following section.

B. Topological phases with LR interactions

In this section, we first identify the possible topological phases in the LR model. Since the gapped topological phases exhibit degenerate edge modes under open boundary conditions (OBCs), we separately calculate the energy spectrum and winding number as a function of h to explicitly demonstrate the possible edge modes at the boundary.

To acquire the winding number, following Ref. [97], we can reformulate the Hamiltonian as follows:

$$H_{\text{LR}} = 4\sum_{k>0} \mathbf{r}_k \cdot \mathbf{s}_k, \tag{3}$$

where $\mathbf{r}_k = (0, y_k, z_k)$ and the pseudospin $\mathbf{s}_k = \frac{1}{2}[c_{-k}^\dagger c_k^\dagger - c_{-k}c_k, i(c_k c_{-k} + c_k^\dagger c_{-k}^\dagger), c_k^\dagger c_k + c_{-k}^\dagger c_{-k} - 1]$. These pseudospin operators satisfy the SU(2) algebra, and the winding number in the auxiliary space (y, z) is defined as

$$\omega = \frac{1}{2\pi}\oint \frac{1}{r^2}(zdy - ydz), \tag{4}$$

where the integral spans over the space (y, z), covering all k values from 0 to 2π. ω serves as a means to distinguish different topological phases, which possess different winding numbers.

To be precise, we calculated the energy spectrum as a function of h for $\alpha > 1$ ($\alpha = 2.2$) and $\alpha < 1$ ($\alpha = 0.8$) under OBCs. As depicted in Figs. 2 (a) and 2(b), we find that when h is less than the critical point, denoted by h_c, there is only one pair of zero-energy edge modes in the energy spectrum [indicated by the red lines in Figs. 2(a) and 2(b)]. Conversely, when $h > h_c$, there are two pairs of zero-energy edge modes in the energy spectrum [indicated by the blues line in Figs. 2(a) and 2(b)]. Similar conclusions can be drawn from Figs. 2(e) and 2(f), which demonstrate the energy spectrum as a function of the state index. Intuitively, we can directly observe that regardless of whether α is large (2.2) or small (0.8), the twofold- (fourfold-) degenerate zero-energy edge mode remain stable against LR interactions before (after) the critical point. Furthermore, we calculated the winding number as a function of h for the same $\alpha = 0.8$ and 2.2, as shown in Figs. 2(c) and 2(d). Before and after the phase-transition point h_c, the winding number changes from 1 to 2, indicating that the number of edge modes changes from one to two pairs, which is consistent with the observations of the energy spectrum (see Appendix B for other interaction powers α). These findings strongly suggest that even with relatively strong LR interactions, the TSC phases of different winding numbers remain stable. In the following section, we will explore the quantum critical behavior between distinct TSC phases and the topological properties of underlying critical points.

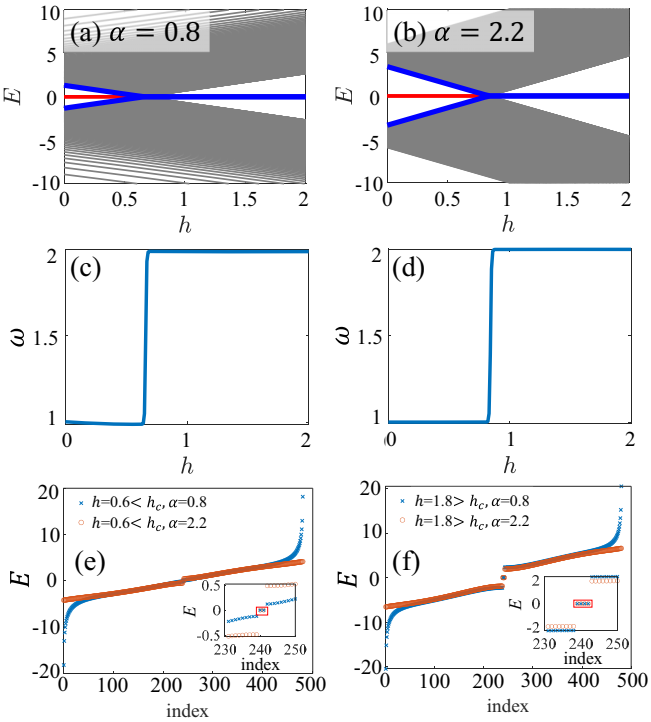

FIG. 2. The energy spectrum as a function of h for the extended Kitaev chain with LR interactions with (a) $\alpha = 0.8$ and (b) 2.2. The winding number as a function of h for the extended Kitaev chain with LR interactions with (c) $\alpha = 0.8$ and (c) 2.2. The energy spectrum as a function of the state index for the LR interacting extended Kitaev chain with (e) $h < h_c$ and (f) $h > h_c$ for $\alpha = 0.8, 2.2$. The red box in the inset shows that there are really two (four) zero-energy edge modes for $\omega = 1$ (2). The energy spectrum calculations are conducted under open boundary conditions, while the winding number calculations are performed under periodic boundary conditions. The simulated system size is $L = 240$.

C. Finite-size scaling and critical exponents

After delineating all the quantum phases in the phase diagram, we shift our attention to the more intriguing quantum phase transitions (QPTs) between these phases and inquire about the scaling and critical exponents at these phase-transition points. As mentioned above, the phase transition between topologically distinct superconducting phases belongs to a topological nontrivial universality class and exhibits robust edge modes on the open boundary. We will investigate whether LR interactions influence the physics of critical edge

modes in the next section. In this section, we determine the critical points and critical exponents for various LR power exponents α through the finite-size scaling of fidelity susceptibility.

The concept of fidelity susceptibility pertains to a system undergoing a continuous phase transition from an ordered to a disordered phase upon tuning the parameter h to a critical value h_c. At this point, the structure of the ground-state wave function changes significantly. The quantum ground-state fidelity $F(h, h+\delta h)$ quantifies the overlapping amplitude between the ground-state wave function at external fields h and $h+\delta h$. Near h_c, $F(h_c, h_c+\delta h) \sim 0$, indicating a drastic change in the ground state. Then, the fidelity susceptibility, defined as the leading term in the fidelity [98,99], is

$$\chi_F(h) = \lim_{\delta h\to 0} \frac{2[1-F(h,h+\delta h)]}{(\delta h)^2} = \frac{1}{4}\sum_{k>0}\left(\frac{\partial\theta_k(h)}{\partial h}\right)^2. \tag{5}$$

For a continuous QPT with a finite system size L, the fidelity susceptibility $\chi_F(h)$ exhibits a peak at a critical point $h_c(L)$, and the value of the quantum critical point h_c^* can be estimated by polynomial fitting $h_c(L) = h_c^* + aL^{-1/\nu}$ [100]. In the vicinity of $h_c(L)$, previous research [101–105] showed that the finite-size scaling behaviors of fidelity susceptibility $\chi_F(h)$ follow

$$\chi_F(h \to h_c(L)) \propto L^{\mu} \tag{6}$$

and

$$L^{-d}\chi_F(h) = L^{(2/\nu)-d} f_{\chi_F}(L^{1/\nu}|h-h_c|), \tag{7}$$

where $\mu(=2+2z-2\Delta_V)$ is the critical adiabatic dimension [98]. Δ_V is the scaling dimension of the local interaction $V(x)$ at h_c^*; ν is correlation-length exponent, and it can be easily computed according to the relation $\nu = 2/\mu$. z is the dynamic exponent, d is the spatial dimension of the system, and f_{χ_F} is an unknown scaling function. Based on Eqs. (6) and (7), the values of the critical exponents ν and μ of the QPT can be determined, and the critical behavior of the LR interacting quantum system can easily be determined. Note that in practice, the critical exponent μ is usually extracted from fidelity susceptibility per site, $\chi_L(f) = \chi_F(h)/L^d$.

The finite-size scaling behavior of the fidelity susceptibility for $\alpha = 0.8$ and 2.2 for different L is presented in Figs. 3(a) and 3(c), which obey $\chi_L(h_c(L)) \propto L^{\mu-1}$ [Eq. (6)] near the second-order QPT critical point. As the system size L increases, the peak position $h_c(L)$ approaches the exact critical point h_c^*, indicating the stability of the critical points regardless of the LR-interaction strength. More precisely, for a LR interacting extended Kitaev chain with $\alpha = 0.8$ and 2.2, h_c^* is determined by polynomially fitting $h_c(L) = h_c^* + aL^{-1/\nu}$ and then extrapolating L to infinity [see insets in Figs. 3(a) and 3(c)]. According to Eq. (7), the fidelity susceptibility follows an exact scaling relation and collapses to a single master curve [Figs. 3(b) and 3(d)], confirming the correctness of the extrapolation. The finite-size scaling behavior of the fidelity susceptibility for other α values is also investigated (see Appendix C for details), and the results are presented

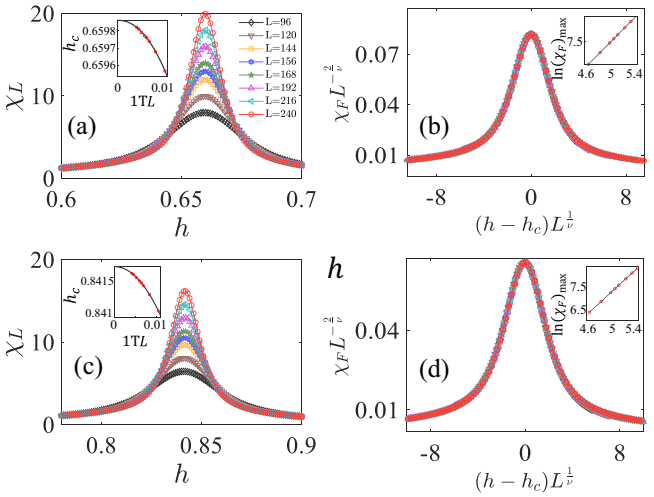

FIG. 3. Fidelity susceptibility per site χ_L of the extended Kitaev chain with LR interactions for (a) $\alpha = 0.8$ and (c) 2.2 with $L = 96, 120, 144, 156, 168, 192, 216, 240$ sites as a function of h. The inset exhibits the extrapolation of the critical point h_c^* for the model. We use polynomial fitting $h_c(L) = h_c^* + aL^{-1/\nu}$ and extrapolate the critical point $h_c^* = 0.65986(1)$ [0.84174(1)] for $\alpha = 0.8$ (2.2). Data collapse of the fidelity susceptibility χ_F for the extended Kitaev chain with (b) $\alpha = 0.8$ and (d) 2.2, where $\nu = 0.9983(2)$ [0.9966(2)] and $h_c^* = 0.65986(1)$ [0.84174(1)] are used for data-collapse plots. The inset shows the maximal fidelity susceptibility per site $\chi_L = \chi_F/L$ as a function of system size L for $\alpha = 0.8$ in (b) and 2.2 in (d). We use polynomial fitting $\chi_F(h_c(L)) = L^{\mu}(c + dL^{-1})$ and extrapolate the critical adiabatic dimension $\mu = 2.0034(3)$ [2.0068(4)] for $\alpha = 0.8$ (2.2).

in Table I. The results show that the QCP shifts to higher h_c^* values as α increases.

The next key question pertains to the critical behavior of LR interacting extended Kitaev chains for different α and whether a critical threshold α_c at which the critical behavior transitions continuously from a LR universality class to a SR one exists. To address this question, we calculate the critical exponents μ and ν of the LR model in the region $0.8 \leqslant \alpha \leqslant 3.0$ for various system sizes L. The fidelity susceptibilities per site, $\chi_L = \chi_F/L$, at the peak position $h_c(L)$ for very strong ($\alpha = 0.8$) and weak ($\alpha = 2.2$) LR interactions are

TABLE I. Critical exponents of the extended Kitaev chain with LR interactions for different α. Critical exponents in the cluster Ising chain ($\alpha = \infty$) are also listed for comparison.

α	h_c^*	ν	μ
0.8	0.65986(1)	0.9983(2)	2.0034(3)
1.0	0.69315(1)	0.9977(2)	2.0046(3)
1.2	0.72383(1)	0.9969(2)	2.0056(3)
1.4	0.75199(1)	0.9966(2)	2.0063(3)
1.8	0.80117(1)	0.9966(2)	2.0068(4)
2.2	0.84174(1)	0.9966(2)	2.0068(4)
2.6	0.87484(1)	0.9967(2)	2.0067(4)
3.0	0.90154(1)	0.9967(2)	2.0066(4)
∞	1.00000	1.00000	2.00000

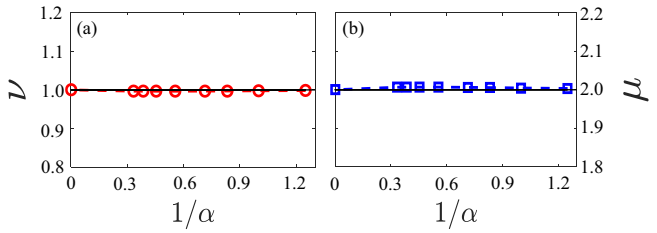

FIG. 4. (a) Critical exponent of the correlation length ν (black dashed line refers to SR Kitaev chain correlation-length exponent $\nu = 1.0$ as a comparison) and (b) critical adiabatic dimension μ (black dashed line refers to SR Kitaev chain critical adiabatic dimension $\mu = 2.0$ as a comparison) as a function of $1/\alpha$ for the extended Kitaev chain with LR interactions.

depicted in Figs. 3(a) and 3(c) (see Appendix C for other LR power exponents α). The adiabatic critical dimension μ can be accurately fitted using a polynomial function of $\chi_L(h_c(L)) = L^{\mu-1}(c + dL^{-1})$, as demonstrated in the insets of Fig. 3(b) and 3(d).

Following Eq. (7), the fidelity susceptibility can be scaled by $L^{-2/\nu}\chi_F$ as a function of $L^{1/\nu}(h - h_c^*)$ in the vicinity of the QCP h_c^*. The critical correlation-length exponent ν is then determined by $\nu = 2/\mu$. Substituting the obtained critical point h_c^* and critical exponent ν into Eq. (7), all fidelity susceptibilities for different L collapse onto a single curve [Figs. 3(b) and 3(d)], indicating the accuracy of the estimated critical point and critical exponent. It is worth noting that the peak of the data collapse is not at zero due to the finite-size effect arising from $h_c(L) = h_c^* + aL^{-1/\nu}$, where $a \neq 0$. The calculations of the critical adiabatic dimension μ and the correlation-length exponent ν for other values of α are presented in Appendix D, and the results for all α are summarized in Table I. As observed in Figs. 4(a) and 4(b), both ν and μ as a function of $1/\alpha$ remain relatively constant and approach the critical exponent of the Kitaev chain in the SR limit, $\nu = 1.0$ and $\mu = 2.0$, respectively [106,107], within the 0.34% error due to finite-size effects (indicated by the black solid line in Fig. 4). Therefore, the critical behavior of the extended Kitaev chain remains unchanged regardless of the strength of the LR interaction, which indicates LR interaction is irrelevant under the renormalization group, and consequently, long-distance properties of the LR model are not significantly modified relative to the SR ground state. We defer the renormalization-group study for the LR interacting extended Kitaev chain to future work. It is worth emphasizing that the above behavior contrasts with typical LR interacting quantum spin chains, which exhibit new LR universality classes [8,9,23].

D. Topological critical edge modes with LR interactions

In the SR limit, a crucial aspect of the phase transition between topologically distinct superconducting phases is the exhibition of topologically protected edge modes, even in the presence of nontrivial coupling between the boundary and the critical bulk modes. Previous studies [13,15] demonstrated that the edge mode in the gapped topological phase remains stable against LR interactions, and a sufficiently strong LR interaction can convert the massless edge mode into a new

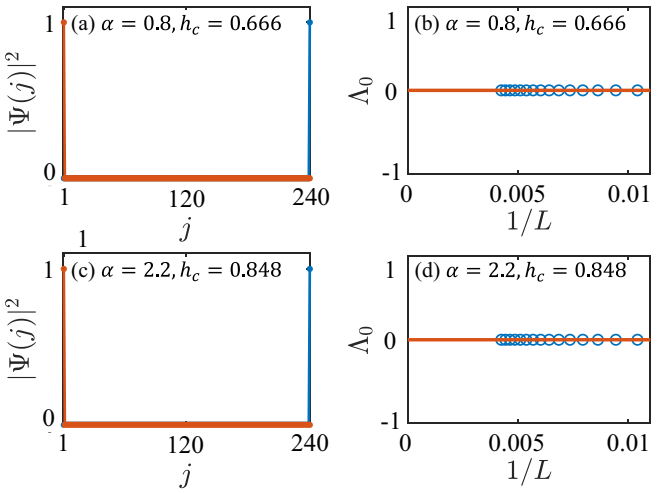

FIG. 5. The zero-energy-state probability distributions at the critical point for $\alpha = 0.8$ (a) and 2.2 (c). Finite size scaling of the edge-mode mass Λ_0 at the critical point for $\alpha = 0.8$ (b) and 2.2 (d). All calculations are conducted under OBCs, and the simulated system size is $L = 240$.

massive one [14,16]. It is natural to inquire whether the edge mode at the topological nontrivial critical point is stable against LR interactions and whether a substantial strong LR interaction can induce novel massive edge modes.

To address these questions, we computed the edge-mode mass Λ_0 and zero-energy-state probability distribution $|\Psi(j)|^2$ at the critical point for the LR model under OBCs (see Appendix E for the calculation details) for both very strong ($\alpha = 0.8$) and weak ($\alpha = 2.2$) LR interactions. As depicted in Figs. 5(a) and 5(c), we observe that no matter how LR the interaction is, the wave function distribution at the critical point exhibits prominent peaks at the boundary, indicating the robustness of the critical edge mode even under very strong LR interactions ($\alpha < 1$). Additionally, to demonstrate the presence of nontrivial topological edge modes within the gapped topological phases, we provide the zero-energy probability distribution for $h < h_c$ and $h > h_c$ in Appendix E for comparison. More importantly, as illustrated in Figs. 5(b) and 5(d), we find that regardless of the LR-interaction strength, the critical-edge-mode mass remains zero in the thermodynamic limit, which is completely different from the LR-interaction-induced massive edge mode observed in gapped topological phases. In Appendix E, we provide additional evidence regarding the critical-edge-mode mass and wave-function distributions for various other α values, further confirming the robustness of the critical massless edge mode against LR interactions.

IV. CONCLUSION AND OUTLOOK

To summarize, we focused on the topologically protected edge modes at the QCPs in LR critical extended Kitaev chains. Specifically, we confirmed the stability of edge modes at critical points between topologically distinct superconducting phases against LR interactions. More importantly, we observed that the edge modes remain massless even when the LR power exponent α is very small, which contrasts with

the massive edge mode induced by LR interactions in the gapped topological phases. Additionally, as a by-product, we determined the critical exponents of the extended Kitaev chain with different LR powers α remaining unchanged through finite-size scaling, aligning with the universality class of the SR Kitaev chain.

From the perspective of experimental realization, numerous studies have explored the properties of LR interacting models, particularly in systems such as trapped ions [108], magnetic impurities [109], and atoms coupled to multimode cavities [110]. Moreover, in the Bogoliubov–de Gennes representation, extended Kitaev chains with LR pairing and hopping can be simulated through Shiba chains [111]. Additionally, the extended LR interacting Kitaev chain can also be experimentally realized through digital simulation using current noisy intermediate-scale superconducting quantum processors [112–114]. A more detailed experimental proposal will be left for future work. Intriguing future inquiries include understanding the underlying physical mechanisms behind the notable differences between LR interacting gapped and gapless topological phases or critical points, as well as their possible higher-dimensional generalizations. Our work could shed new light on the interplay between LR interactions (frustrated) and the gapless topological phases of matter.

ACKNOWLEDGMENTS

This work is supported by the start-up grant XRC-23102 and Student Research Training Program No. 30250 of Fuzhou University.

APPENDIX A: ANALYTICAL CALCULATIONS DETAILS

In this Appendix, we provide details of the analytic derivation presented in the main text. This derivation relies on the integrability of the LR fermionic Hamiltonian given in Eq. (1), which is obtained through Fourier transformation: $c_k = \frac{1}{\sqrt{L}}\sum_{j=1}^{L} c_j e^{-ikj}$, where $k = \pm\frac{(2n-1)\pi}{L}$, $n = 0, 1, 2, \ldots, \frac{L}{2}$,

$$H_{\mathrm{LR}} = \sum_k [iy_k(c_k c_{-k} + c_k^\dagger c_{-k}^\dagger) + z_k(c_k^\dagger c_k + c_{-k}^\dagger c_{-k} - 1)]. \tag{A1}$$

Here, $y_k = -h\sin(2k) - \Delta f_\alpha(k)$, and $z_k = -h\cos(2k) - \Delta g_\alpha(k)$, with $f_\alpha(k) = \sum_l \sin(kl)/d_l^\alpha$ and $g_\alpha(k) = \sum_l \cos(kl)/d_l^\alpha$. Using the Bogoliubov transformation, defined as

$$\gamma_k = \cos\left(\frac{\theta_k}{2}\right)c_k - i\sin\left(\frac{\theta_k}{2}\right)c_{-k}^\dagger, \tag{A2}$$

$$\gamma_k^\dagger = \cos\left(\frac{\theta_k}{2}\right)c_k^\dagger + i\sin\left(\frac{\theta_k}{2}\right)c_{-k}, \tag{A3}$$

with

$$\tan(\theta_k) = -\frac{y_k}{z_k}, \tag{A4}$$

the Hamiltonian can be diagonalized as

$$H_{\mathrm{LR}} = \sum_{k>0}\epsilon_k\left(\gamma_k^\dagger\gamma_k - \frac{1}{2}\right), \tag{A5}$$

where

$$\epsilon_k = 4\sqrt{y_k^2 + z_k^2}. \tag{A6}$$

Finally, the ground state $|G\rangle$ of the model is given by

$$|G\rangle = \prod_{k>0}\left[\cos\left(\frac{\theta_k}{2}\right) + i\sin\left(\frac{\theta_k}{2}\right)c_k^\dagger c_{-k}^\dagger\right]|\mathrm{Vac}\rangle, \tag{A7}$$

where $|\mathrm{Vac}\rangle$ denotes the vacuum state of the c fermion.

Once the ground state and energy spectrum of the model are obtained, we can calculate different types of physical quantities to study the various phases and phase transitions in the phase diagram.

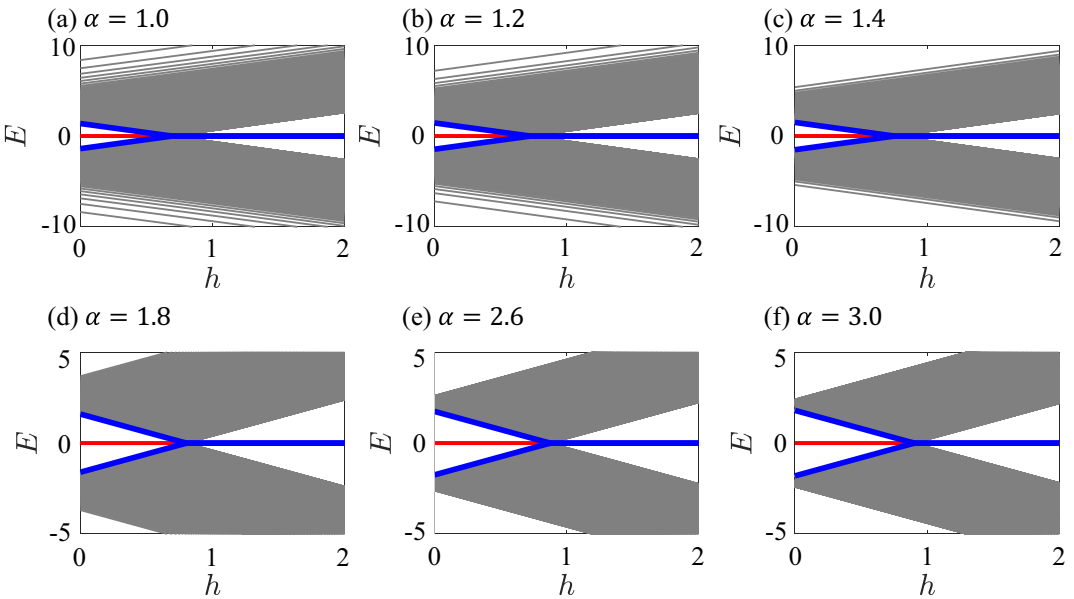

FIG. 6. Energy spectrum for (a) $\alpha = 1.0$, (b) $\alpha = 1.2$, (c) $\alpha = 1.4$, (d) $\alpha = 1.8$, (e) $\alpha = 2.6$, and (f) $\alpha = 3.0$ and fixed site $L = 240$ as a function of parameter h.

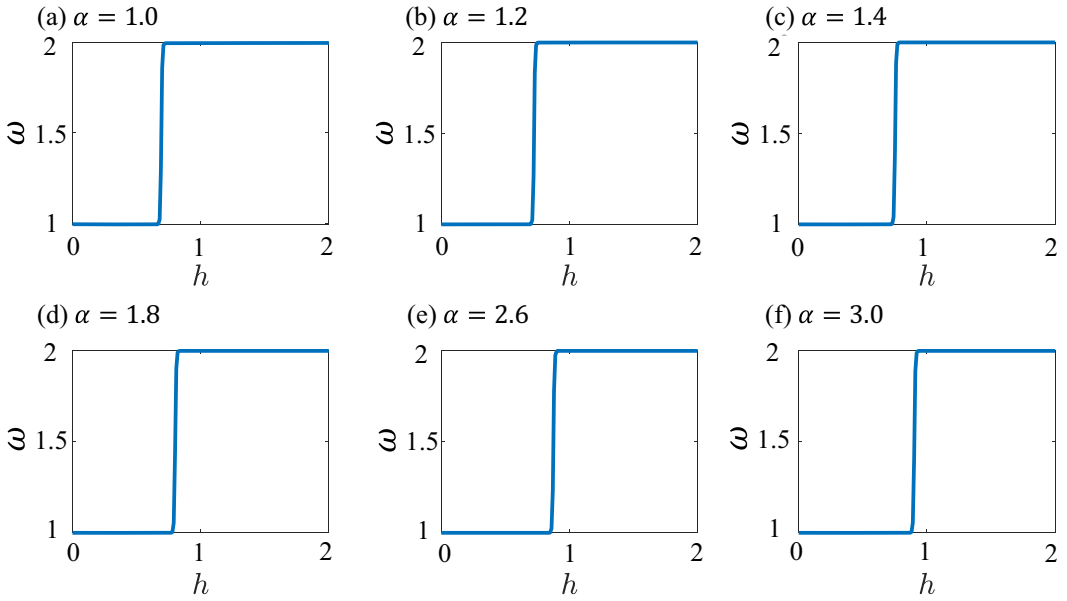

FIG. 7. The winding number as a function of h for the extended Kitaev chain with LR interactions with (a) $\alpha = 1.0$, (b) 1.2, (c) 1.4, (d) 1.8, (e) 2.6, and (f) 3.0. The simulated system size is $L = 240$.

APPENDIX B: ENERGY SPECTRUM AND WINDING NUMBER FOR OTHER INTERACTION POWERS

In this Appendix, we provide additional data demonstrating the energy spectrum under OBCs and the winding number for other interaction powers α.

The Hamiltonian (1) under OBCs can be diagonalized as $H = \sum_{n=1}^{L} \Lambda_n \eta_n^\dagger \eta_n$ through a canonical Bogoliubov transformation by introducing the fermionic operators η_n and $\eta_n^\dagger$,

$$\eta_n = \sum_j^N (u_{n,j}^* c_j + v_{n,j} c_j^\dagger), \quad \eta_n^\dagger = \sum_j^N (u_{n,j} c_j^\dagger + v_{n,j}^* c_j), \quad \text{(B1)}$$

where $u_{n,j}$ and $v_{n,j}$ denote the two components of the wave function at site j, n is the energy band index, and Λ_n

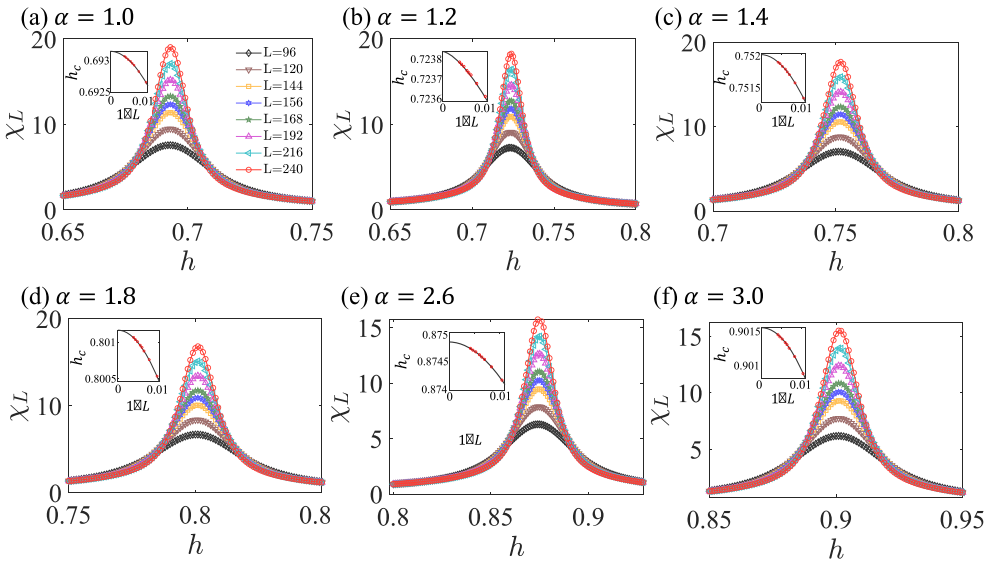

FIG. 8. The fidelity susceptibility per site χ_L is plotted as a function of the parameter h for (a) $\alpha = 1.0$, (b) $\alpha = 1.2$, (c) $\alpha = 1.4$, (d) $\alpha = 1.8$, (e) $\alpha = 2.6$, and (f) $\alpha = 3.0$. The data include various lattice sizes $L = 96$, 120, 144, 156, 168, 192, 216, 240. Additionally, the insets present a finite-size scaling analysis of the critical point for each α value as a function of the lattice size L. To determine the critical point in the thermodynamic limit, we utilize the fitting formula $h_c(L) = h_c^* + aL^{-1/\nu}$, where h_c^* represents the critical point in the thermodynamic limit.

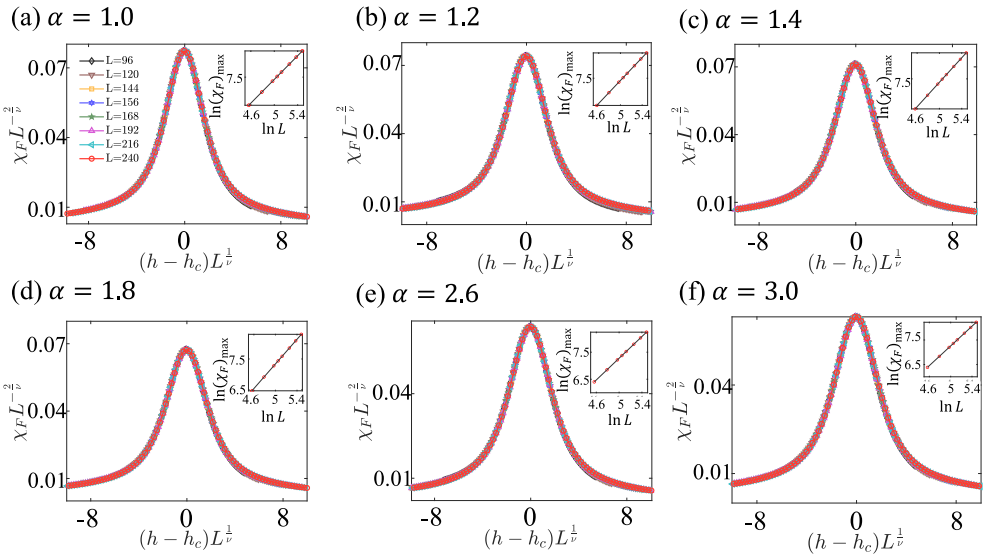

FIG. 9. Data-collapse analysis of fidelity susceptibility χ_F for various scenarios with different LR power exponents α, including (a) $\alpha = 1.0$, (b) $\alpha = 1.2$, (c) $\alpha = 1.4$, (d) $\alpha = 1.8$, (e) $\alpha = 2.6$, and (f) $\alpha = 3.0$. Additionally, we performed finite-size scaling for the maximum fidelity susceptibility, as illustrated in the inset. To obtain the critical exponent μ, we employed the fitting formula $\chi_F(h_c(L)) = L^{\mu}(c + dL^{-1})$ for our analysis.

represents the eigenstate energy. The Schrödinger equation $H|\Psi_n\rangle = E_n|\Psi_n\rangle$ can be written as

$$\begin{pmatrix} A & B \\ -B^* & -A^T \end{pmatrix} \begin{pmatrix} u_{n,i} \\ v^*_{n,i} \end{pmatrix} = E_n \begin{pmatrix} u_{n,i} \\ v^*_{n,i} \end{pmatrix}, \tag{B2}$$

where $A(B)$ is an $N \times N$ symmetric (antisymmetric) matrix, E_n is the energy spectrum, and n is the state index.

Like in the main text, the energy spectra as a function of the parameter h for different values of α, $\alpha = 1.0$, $\alpha = 1.2$, $\alpha = 1.4$, $\alpha = 1.8$, $\alpha = 2.6$, and $\alpha = 3.0$, with a fixed system size of $L = 240$, are illustrated in Figs. 6(a)–6(f), respectively. It is evident that there is only one pair of zero-energy edge modes in the energy spectrum when $h < h_c$, and two pairs of zero-energy edge modes emerge when $h > h_c$ (see Fig. 6).

On the other hand, the winding numbers for various values of α, $\alpha = 1.0$, $\alpha = 1.2$, $\alpha = 1.4$, $\alpha = 1.8$, $\alpha = 2.6$, and $\alpha = 3.0$, are plotted in Figs. 7(a)–7(f), respectively, as a function of the parameter h for system size $L = 240$. It is evident that regardless of α, the TSC phases with different winding numbers remain stable. Moreover, before and after the phase-transition point h_c, the winding number changes from 1 to 2, indicating that the number of edge modes changes from one to two pairs, which is consistent with the observations of the energy spectrum.

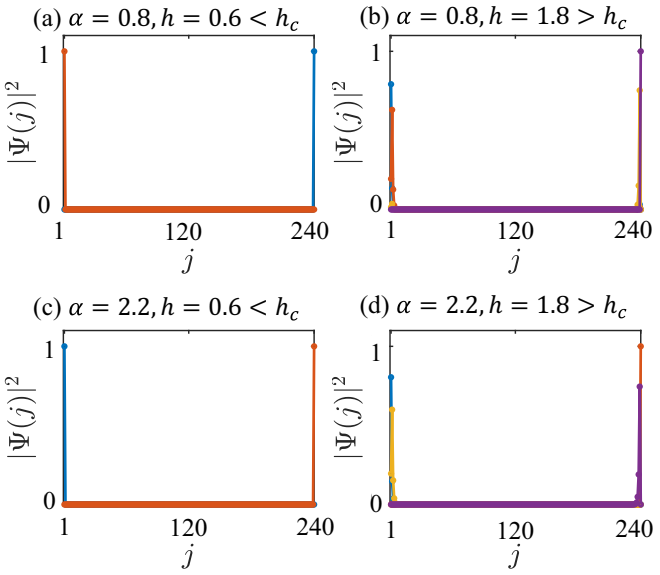

FIG. 10. The zero-energy-state probability distribution with different LR powers α for (a) and (c) $h < h_c$ (a pair of edge modes are shown) and (b) and (d) $h > h_c$ (two pairs of edge modes are shown). All calculations are conducted under OBCs, and the simulated system size is $L = 240$.

APPENDIX C: FIDELITY SUSCEPTIBILITY AND QUANTUM CRITICAL POINTS FOR OTHER INTERACTION POWERS

In this Appendix, we provide additional data to illustrate the fidelity susceptibility χ_L and the fitting of the quantum critical points for other interaction powers α.

Like in the main text, the fidelity susceptibility per site is presented in Figs. 8(a)–8(f) for $\alpha = 1.0$, $\alpha = 1.2$, $\alpha = 1.4$, $\alpha = 1.8$, $\alpha = 2.6$, and $\alpha = 3.0$, respectively. The data are plotted as a function of the parameter h for lattice sizes of $L = 96, 120, 144, 156, 168, 192, 216, 240$ sites. The insets in Fig. 8 illustrate the finite-size scaling analysis for the critical point, considering the same range of α values, as a function of the lattice size L. Utilizing the fitting formula $h_c(L) = h_c^* + aL^{-1/\nu}$, we determine the critical point in the thermodynamic limit, denoted as h_c^*, and find that the quantum critical point shifts to higher h_c^* values as α increases.

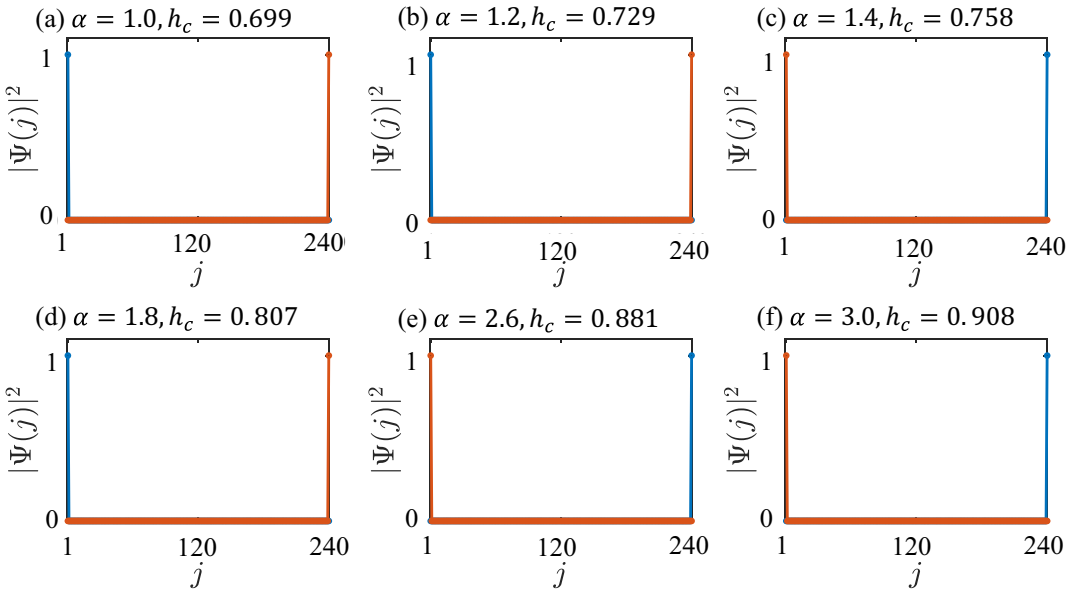

FIG. 11. The zero-energy-state probability distribution at the critical point for (a) $\alpha = 1.0$, (b) $\alpha = 1.2$, (c) $\alpha = 1.4$, (d) $\alpha = 1.8$, (e) $\alpha = 2.6$, (f) $\alpha = 3.0$, and fixed system sizes $L = 240$.

APPENDIX D: DATA COLLAPSES AND CRITICAL EXPONENTS FOR OTHER INTERACTION POWERS

In this Appendix, we provide additional data to extrapolate critical exponents and demonstrate the accuracy of the estimated critical point and critical exponent for other interaction powers α.

Like in the main text, data collapse of the fidelity susceptibility χ_F for $\alpha = 1.0$, $\alpha = 1.2$, $\alpha = 1.4$, $\alpha = 1.8$, $\alpha = 2.6$, and $\alpha = 3.0$, with different lattice sizes L, is shown in Figs. 9(a)–9(f), respectively. All fidelity susceptibilities for different L collapse onto a single curve, indicating the accuracy of the estimated critical point and critical exponent. To determine the critical adiabatic dimension μ, we also performed finite-size scaling for the maximum of the fidelity susceptibility for $\alpha = 1.0$, $\alpha = 1.2$, $\alpha = 1.4$, $\alpha = 1.8$, $\alpha = 2.6$, and $\alpha = 3.0$ as a function of lattice size L, as shown in the insets in Figs. 9(a)–9(f), respectively. We used the fitting formula $\chi_F(h_c(L)) = L^{\mu}(c + dL^{-1})$ to obtain the critical

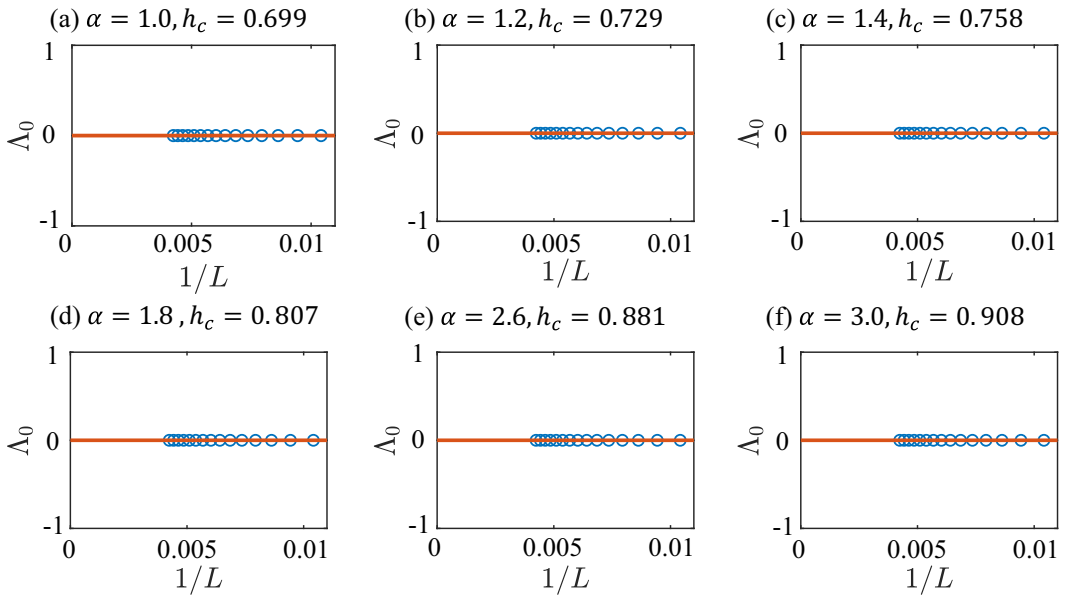

FIG. 12. The critical-edge-mode mass as a function of inverse system size $1/L$ for (a) $\alpha = 1.0$, (b) $\alpha = 1.2$, (c) $\alpha = 1.4$, (d) $\alpha = 1.8$, (e) $\alpha = 2.6$, and (f) $\alpha = 3.0$.

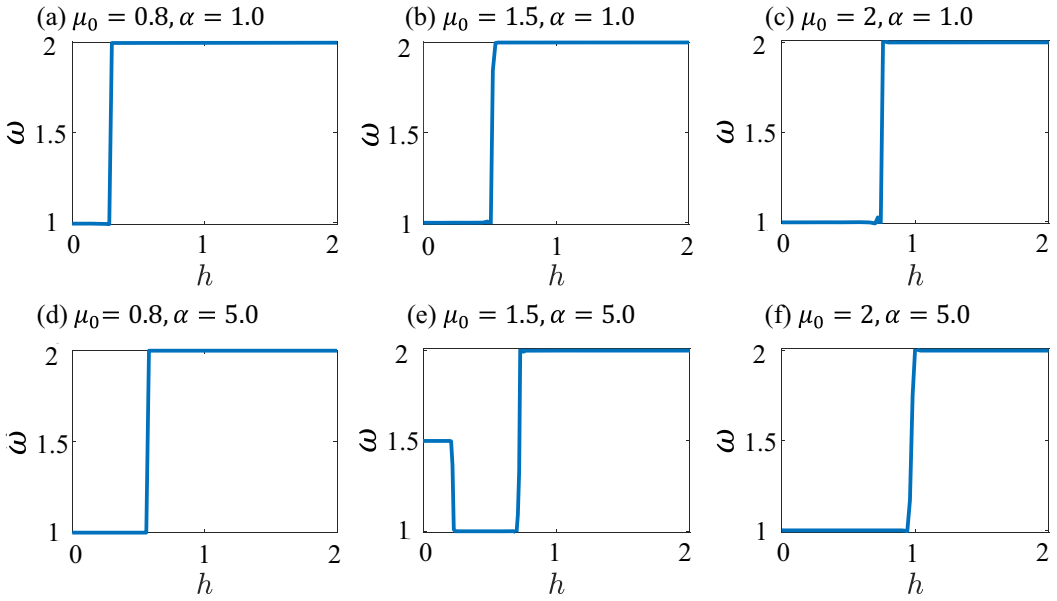

FIG. 13. The winding number as a function of h for the LR interacting extended Kitaev chain with nonzero chemical potential with (a) $\alpha = 1.0$, $\mu_0 = 0.8$, (b) $\alpha = 1.0$, $\mu_0 = 1.5$, (c) $\alpha = 1.0$, $\mu_0 = 2.0$, (d) $\alpha = 5.0$, $\mu_0 = 0.8$, (e) $\alpha = 5.0$, $\mu_0 = 1.5$, and (f) $\alpha = 5.0$, $\mu_0 = 2.0$. The simulated system size is $L = 240$.

adiabatic dimension μ. The results exhibit that the critical adiabatic dimension μ as a function of $1/\alpha$ remains relatively constant and approaches the critical exponent of the Kitaev chain in the SR limit.

APPENDIX E: THE ZERO-ENERGY-STATE PROBABILITY DISTRIBUTION AND EDGE-MODE MASS FOR OTHER INTERACTION POWERS

In this Appendix, we provide more evidence to verify the topological properties at and away from the QCPs. Specifically, according to Eq. (B2), the zero-energy-state probability distributions can be computed as $|\Psi_{n,j}|^2 = |u_{n,j}|^2 + |v_{n,j}|^2$. To directly demonstrate the degenerate edge states in topological superconducting phases, we present the zero-energy-state probability distributions before and after the critical points for different values of α, as depicted in Fig. 10(a) for $\alpha = 0.8$ and Fig. 10(b) for $\alpha = 2.2$. The results unambiguously show the twofold- (fourfold-) degenerate edge modes within the topological superconducting phases with winding number $\omega = 1$ (2), which is consistent with previous numerical results.

More importantly, as illustrated in the main text, the zero-energy edge-mode distributions at the critical points for different values of α, $\alpha = 1.0$, $\alpha = 1.2$, $\alpha = 1.4$, $\alpha = 1.8$, $\alpha = 2.6$, and $\alpha = 3.0$, with a fixed lattice size of $L = 240$ are depicted in Figs. 11(a)–11(f), respectively. We observe that regardless of the strength of the LR interaction, the zero-energy-state probability distribution at the critical point consistently exhibits prominent peaks at the boundary. This observation underscores the robustness of the

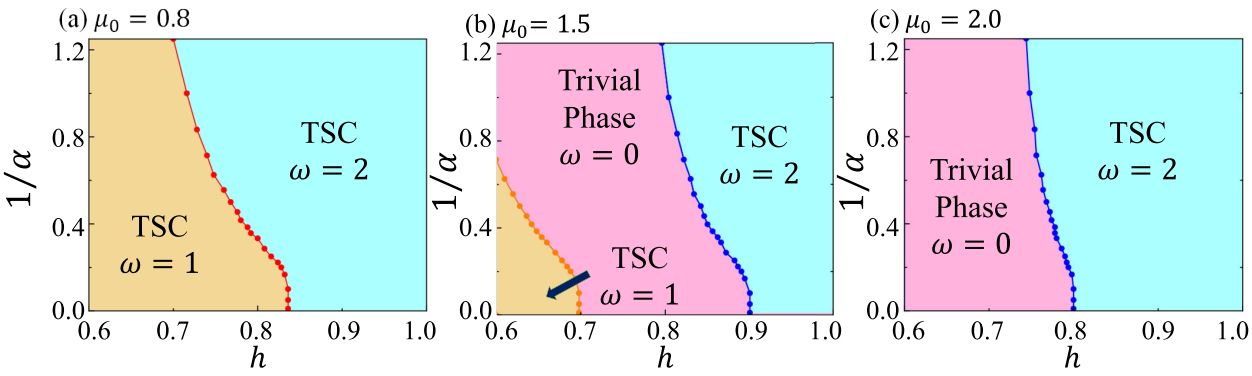

FIG. 14. The global phase diagram in the extended Kitaev chain with long-range interactions as a function of the long-range power exponent α and the driven parameter h for typical values of the chemical potential: (a) $\mu_0 = 0.8$, (b) $\mu_0 = 1.5$, and (c) $\mu_0 = 2.0$. The diagrams delineate the topological superconductor with winding number ω, denoted as the TSC $\omega = 1$ phase (brown region), the TSC $\omega = 2$ phase (light blue region), and trivial phase ($\omega = 0$; light purple region). The red, orange, and blue points mark the critical points corresponding to different phases, and the red, orange, and blue lines form the critical lines between the two phases.

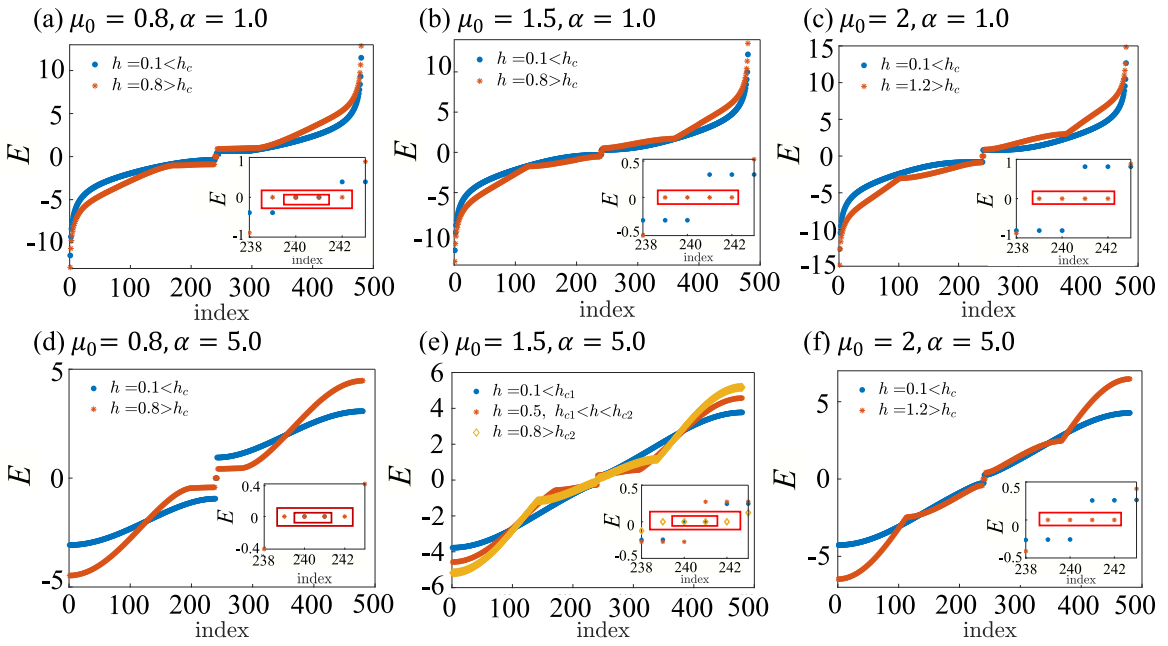

FIG. 15. The energy spectrum as a function of the state index for the LR interacting extended Kitaev chain with nonzero chemical potential with (a) $\alpha = 1.0$, $\mu_0 = 0.8$, (b) $\alpha = 1.0$, $\mu_0 = 1.5$, (c) $\alpha = 1.0$, $\mu_0 = 2.0$, (d) $\alpha = 5.0$, $\mu_0 = 0.8$, (e) $\alpha = 5.0$, $\mu_0 = 1.5$, and (f) $\alpha = 5.0$, $\mu_0 = 2.0$. The red box in the inset shows that there are really two (four) zero-energy edge modes for $\omega = 1$ (2) and no zero-energy edge modes for $\omega = 0$. The simulated system size is $L = 240$.

twofold-degenerate critical edge mode even under very strong LR interactions.

On the other hand, like for the LR gapped topological phase, to explore whether LR interaction may turn the massless edge mode into a massive one, we define the mass gap at finite size L as $\Lambda_0 = \min_n \Lambda_n$. The edge-mode masses at the critical point as a function of the inverse system size $1/L$ for $\alpha = 1.0$, $\alpha = 1.2$, $\alpha = 1.4$, $\alpha = 1.8$, $\alpha = 2.6$, and $\alpha = 3.0$, are shown in Figs. 12(a)–12(f), respectively. We observe that the edge-mode mass remains zero in the thermodynamic limit even with very small α, which is entirely different from the emergence of massive edge modes in gapped topological phases.

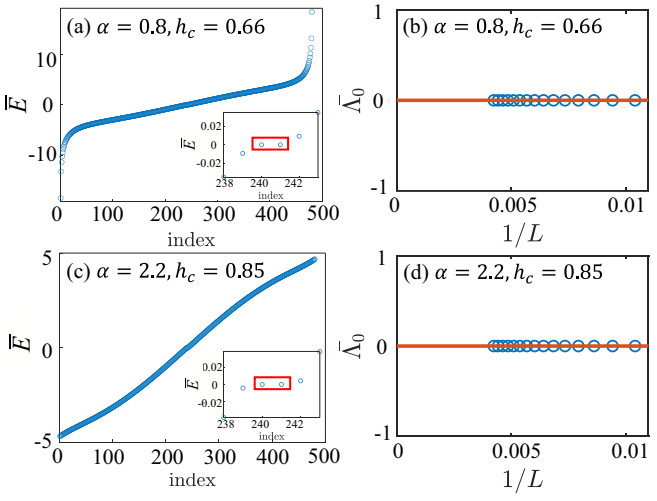

FIG. 16. The average energy spectrum $\bar{E}$ with the state index for the extended Kitaev chain with $h = h_c$ for (a) $\alpha = 0.8$ and (c) $\alpha = 2.2$. The inset shows that there are really two zero-energy states at the critical point. Finite-size scaling of the average edge-mode mass $\bar{\Lambda}_0$ at the critical point for (b) $\alpha = 0.8$ and (d) $\alpha = 2.2$. All calculations were conducted under OBCs with $W = 0.1$. We performed disorder averaging over 3000 samples. The error is too small to be seen on this scale.

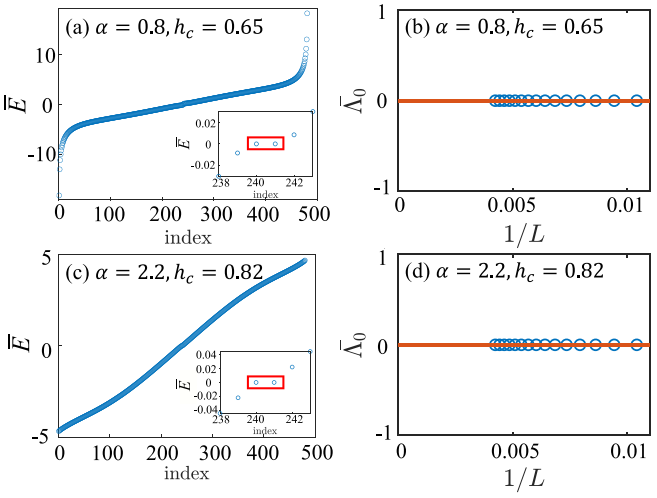

FIG. 17. The average energy spectrum $\bar{E}$ with the state index for the extended Kitaev chain with $h = h_c$ for (a) $\alpha = 0.8$ and (c) $\alpha = 2.2$. The inset shows that there are really two zero-energy states at the critical point. (b) Finite-size scaling of the average edge-mode mass $\bar{\Lambda}_0$ at the critical point for (b) $\alpha = 0.8$ and (d) $\alpha = 2.2$. All calculations were conducted under OBCs with $W = 0.4$. We performed disorder averaging over 10 000 samples. The error is too small to be seen on this scale.

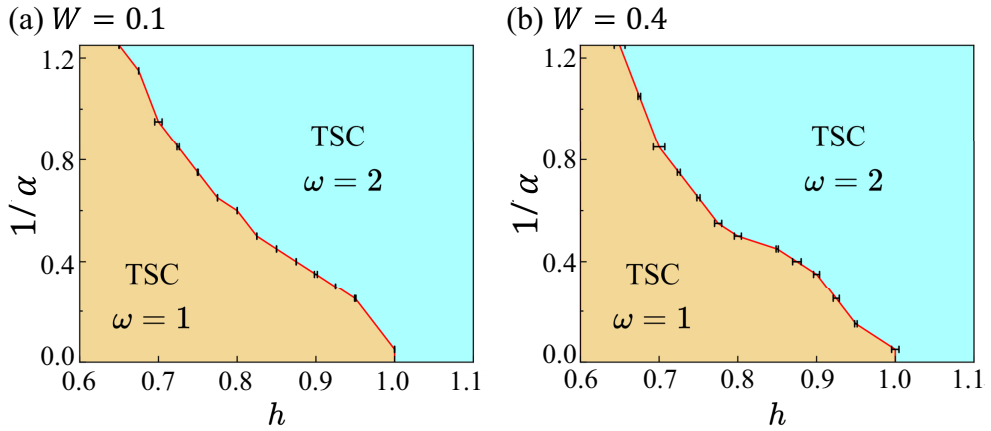

FIG. 18. Global phase diagram illustrating the extended Kitaev chain with long-range interactions as a function of the long-range power exponent α and the driven parameter h with typical on-site disorder (a) $W = 0.1$ and (b) 0.4. Even with finite on-site disorder, the phase diagram delineates the topological superconductor with winding number ω, denoted as the TSC $\omega = 1$ phase (brown region) and the TSC $\omega = 2$ phase (light blue region). The red line forms the critical line between the two phases.

APPENDIX F: TOPOLOGICAL PHASE DIAGRAM WITH UNIFORM AND RANDOM CHEMICAL POTENTIAL

In this Appendix, we provide additional numerical evidence and a brief discussion of the influence of the uniform and random chemical potential μ_0.

We first explore the influence of the uniform chemical potential by setting $\mu_j = \mu_0$ in Eq. (1). In this case, we follow the method in Appendix A and analytically calculate various physical quantities with a modified $z_k = -h\cos(2k) - \Delta g_\alpha(k) - \mu_0/2$. Specifically, we calculated the winding number, as shown in Fig. 13, to construct the global phase diagram in Fig. 14 for typical values of μ_0. Our systematic numerical results unambiguously demonstrate that, with a small value of chemical potential, the topologically nontrivial superconducting phases with different winding numbers (1 and 2) persist in the phase diagram (see Fig. 15), along with the topologically nontrivial quantum critical point (red points in Fig. 14) for lower h compared to the $\mu_0 = 0$ case, which is

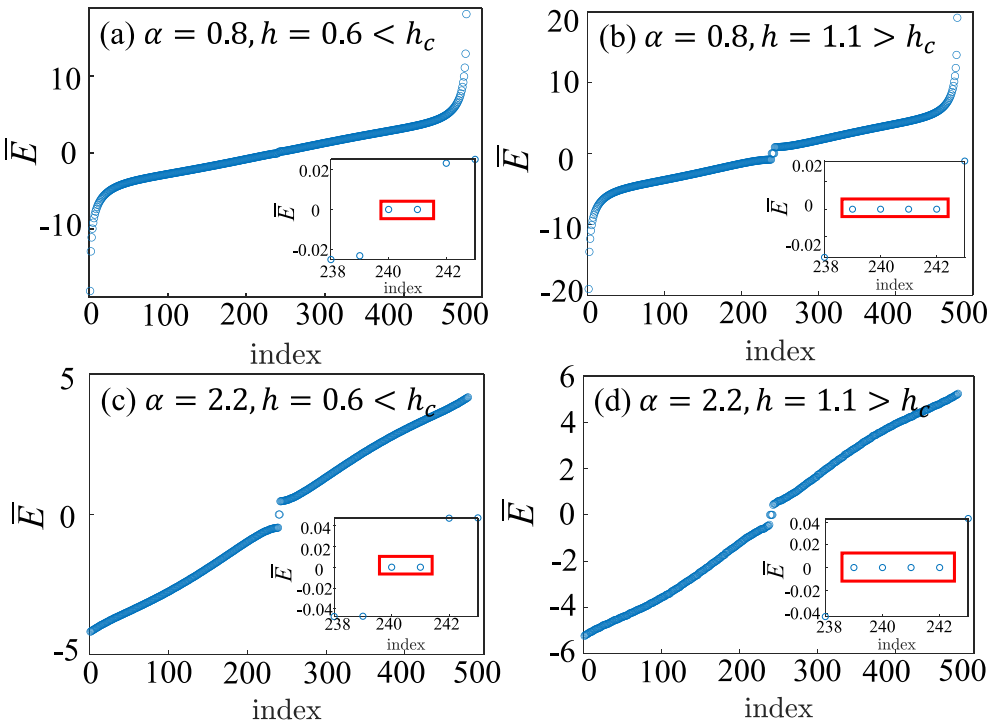

FIG. 19. The average energy spectrum $\bar{E}$ with the state index for the extended Kitaev chain with $W = 0.1$ (a) before and (b) after the critical point and with $W = 0.4$ (c) before and (d) after the critical point. The inset shows that there are really two zero-energy states in the TSC $\omega = 1$ phase (brown region) and four zero-energy states in the TSC $\omega = 2$ phase (light blue region). All calculations were conducted under OBCs with $L = 240$. The error is too small to be seen on this scale.

a key point of our work. However, we observe that for larger values of chemical potential ($\mu_0 > 1.0$), a trivial phase with $\omega = 0$ (light purple region in Fig. 14) emerges in the phase diagram, alongside topological superconducting phases with $\omega = 1, 2$, splitting the original topologically nontrivial critical line into two topologically trivial quantum critical lines (blue and orange points in Fig. 14). These new numerical results further provide compelling evidence that the topologically nontrivial quantum critical point between different topological superconductors remains robust against small chemical potential.

To verify the generality of our results, we also investigate the effect of random disorder on the topological phase diagram. Specifically, we randomly set the on-site chemical potential over sites within the range $[-W, W]$, where W is the strength of on-site disorder. We performed disorder averaging over 3000 samples for $W = 0.1$ and 10 000 samples for $W = 0.4$, with a simulated system size of $L = 240$. To demonstrate the topological stability of the critical edge mode against disorder, we present numerical results with typical disorder strengths ($W = 0.1, 0.4$) showing the average energy spectrum as a function of the state index and the finite-size scaling of the average edge-mode mass at the critical point in Figs. 16 and 17. The results unambiguously demonstrate that the critical edge mode remains stable and massless against on-site disorder. Furthermore, we provide the global phase diagram with typical on-site disorder to illustrate the generality of our conclusion in Fig. 18. Despite the presence of disorder, the structure of the phase diagram remains similar to the clean case, with the topological superconducting phase (see also Fig. 19) and the topological nontrivial quantum critical point remaining robust against weak disorder. A more detailed discussion of the effects of disorder is very involved, and we will definitely delve into this interesting topic in the future.

[1] S. Sachdev, *Quantum Phase Transitions*, 2nd ed. (Cambridge University Press, Cambridge, 2011).

[2] S. Sachdev, *Quantum Phases of Matter* (Cambridge University Press, Cambridge, 2023).

[3] J. Cardy, *Scaling and Renormalization in Statistical Physics* (Cambridge University Press, Cambridge, 1996).

[4] E. Fradkin, *Field Theories of Condensed Matter Physics* (Cambridge University Press, Cambridge, 2013).

[5] N. Defenu, T. Donner, T. Macrì, G. Pagano, S. Ruffo, and A. Trombettoni, Long-range interacting quantum systems, Rev. Mod. Phys. **95**, 035002 (2023).

[6] S. Maity, U. Bhattacharya, and A. Dutta, One-dimensional quantum many body systems with long-range interactions, J. Phys. A **53**, 013001 (2020).

[7] Z.-X. Gong, M. Foss-Feig, F. G. S. L. Brandão, and A. V. Gorshkov, Entanglement area laws for long-range interacting systems, Phys. Rev. Lett. **119**, 050501 (2017).

[8] N. Defenu, A. Trombettoni, and S. Ruffo, Criticality and phase diagram of quantum long-range O(N) models, Phys. Rev. B **96**, 104432 (2017).

[9] N. Defenu, A. Trombettoni, and A. Codello, Fixed-point structure and effective fractional dimensionality for O(N) models with long-range interactions, Phys. Rev. E **92**, 052113 (2015).

[10] A. Codello, N. Defenu, and G. D'Odorico, Critical exponents of $O(N)$ models in fractional dimensions, Phys. Rev. D **91**, 105003 (2015).

[11] P. Bruno, Absence of spontaneous magnetic order at nonzero temperature in one- and two-dimensional Heisenberg and XY systems with long-range interactions, Phys. Rev. Lett. **87**, 137203 (2001).

[12] M. F. Maghrebi, Z.-X. Gong, and A. V. Gorshkov, Continuous symmetry breaking in 1D long-range interacting quantum systems, Phys. Rev. Lett. **119**, 023001 (2017).

[13] D. Vodola, L. Lepori, E. Ercolessi, A. V. Gorshkov, and G. Pupillo, Kitaev chains with long-range pairing, Phys. Rev. Lett. **113**, 156402 (2014).

[14] D. Vodola, L. Lepori, E. Ercolessi, and G. Pupillo, Long-range Ising and Kitaev models: Phases, correlations and edge modes, New J. Phys. **18**, 015001 (2015).

[15] O. Viyuela, D. Vodola, G. Pupillo, and M. A. Martin-Delgado, Topological massive Dirac edge modes and long-range superconducting Hamiltonians, Phys. Rev. B **94**, 125121 (2016).

[16] L. Lepori, D. Vodola, G. Pupillo, G. Gori, and A. Trombettoni, Effective theory and breakdown of conformal symmetry in a long-range quantum chain, Ann. Phys. (NY) **374**, 35 (2016).

[17] M. E. Fisher, S.-K. Ma, and B. G. Nickel, Critical exponents for long-range interactions, Phys. Rev. Lett. **29**, 917 (1972).

[18] E. Brezin, G. Parisi, and F. Ricci-Tersenghi, The crossover region between long-range and short-range interactions for the critical exponents, J. Stat. Phys. **157**, 855 (2014).

[19] M. C. Angelini, G. Parisi, and F. Ricci-Tersenghi, Relations between short-range and long-range Ising models, Phys. Rev. E **89**, 062120 (2014).

[20] C. Behan, L. Rastelli, S. Rychkov, and B. Zan, Long-range critical exponents near the short-range crossover, Phys. Rev. Lett. **118**, 241601 (2017).

[21] C. Behan, L. Rastelli, S. Rychkov, and B. Zan, A scaling theory for the long-range to short-range crossover and an infrared duality, J. Phys. A **50**, 354002 (2017).

[22] X.-J. Yu, S. Yang, J.-B. Xu, and L. Xu, Fidelity susceptibility as a diagnostic of the commensurate-incommensurate transition: A revisit of the programmable Rydberg chain, Phys. Rev. B **106**, 165124 (2022).

[23] X.-J. Yu, C. Ding, and L. Xu, Quantum criticality of a $\mathbb{Z}_3$-symmetric spin chain with long-range interactions, Phys. Rev. E **107**, 054122 (2023).

[24] S. Yang, Z. Pan, D.-C. Lu, and X.-J. Yu, Emergent self-duality in a long-range critical spin chain: From deconfined criticality to first-order transition, Phys. Rev. B **108**, 245152 (2023).

[25] I. Bloch, J. Dalibard, and W. Zwerger, Many-body physics with ultracold gases, Rev. Mod. Phys. **80**, 885 (2008).

[26] H. Ritsch, P. Domokos, F. Brennecke, and T. Esslinger, Cold atoms in cavity-generated dynamical optical potentials, Rev. Mod. Phys. **85**, 553 (2013).

[27] F. Mivehvar, F. Piazza, T. Donner, and H. Ritsch, Cavity QED with quantum gases: New paradigms in many-body physics, Adv. Phys. **70**, 1 (2021).

[28] T. D. Ladd, F. Jelezko, R. Laflamme, Y. Nakamura, C. Monroe, and J. L. O'Brien, Quantum computers, Nature (London) **464**, 45 (2010).

[29] C. Monroe, W. C. Campbell, L.-M. Duan, Z.-X. Gong, A. V. Gorshkov, P. W. Hess, R. Islam, K. Kim, N. M. Linke, G. Pagano, P. Richerme, C. Senko, and N. Y. Yao, Programmable quantum simulations of spin systems with trapped ions, Rev. Mod. Phys. **93**, 025001 (2021).

[30] H. Bernien *et al.*, Probing many-body dynamics on a 51-atom quantum simulator, Nature (London) **551**, 579 (2017).

[31] S. Ebadi *et al.*, Quantum phases of matter on a 256-atom programmable quantum simulator, Nature (London) **595**, 227 (2021).

[32] A. Keesling *et al.*, Quantum Kibble–Zurek mechanism and critical dynamics on a programmable Rydberg simulator, Nature (London) **568**, 207 (2019).

[33] G. Semeghini *et al.*, Probing topological spin liquids on a programmable quantum simulator, Science **374**, 1242 (2021).

[34] X. Chen, Z.-C. Gu, Z.-X. Liu, and X.-G. Wen, Symmetry-protected topological orders in interacting bosonic systems, Science **338**, 1604 (2012).

[35] X.-G. Wen, Choreographed entanglement dances: Topological states of quantum matter, Science **363**, eaal3099 (2019).

[36] X.-G. Wen, Colloquium: Zoo of quantum-topological phases of matter, Rev. Mod. Phys. **89**, 041004 (2017).

[37] X. Chen, Z.-C. Gu, Z.-X. Liu, and X.-G. Wen, Symmetry protected topological orders and the group cohomology of their symmetry group, Phys. Rev. B **87**, 155114 (2013).

[38] T. Senthil, Symmetry-protected topological phases of quantum matter, Annu. Rev. Condens. Matter Phys. **6**, 299 (2015).

[39] X.-J. Yu, S.-H. Shi, L. Xu, and Z.-X. Li, Emergence of competing orders and possible quantum spin liquid in SU(N) fermions, Phys. Rev. Lett. **132**, 036704 (2024).

[40] H. C. Wu, H. S. Xu, L. C. Xie, and L. Jin, Edge state, band topology, and time boundary effect in the fine-grained categorization of Chern insulators, Phys. Rev. Lett. **132**, 083801 (2024).

[41] M. Z. Hasan and C. L. Kane, Colloquium: Topological insulators, Rev. Mod. Phys. **82**, 3045 (2010).

[42] X.-L. Qi and S.-C. Zhang, Topological insulators and superconductors, Rev. Mod. Phys. **83**, 1057 (2011).

[43] E. Witten, Three lectures on topological phases of matter, Riv. Nuovo Cimento **39**, 313 (2016).

[44] F. Pollmann, A. M. Turner, E. Berg, and M. Oshikawa, Entanglement spectrum of a topological phase in one dimension, Phys. Rev. B **81**, 064439 (2010).

[45] L. Fidkowski and A. Kitaev, Topological phases of fermions in one dimension, Phys. Rev. B **83**, 075103 (2011).

[46] F. Pollmann and A. M. Turner, Detection of symmetry-protected topological phases in one dimension, Phys. Rev. B **86**, 125441 (2012).

[47] R. Verresen, R. Thorngren, N. G. Jones, and F. Pollmann, Gapless topological phases and symmetry-enriched quantum criticality, Phys. Rev. X **11**, 041059 (2021).

[48] X.-J. Yu, R.-Z. Huang, H.-H. Song, L. Xu, C. Ding, and L. Zhang, Conformal boundary conditions of symmetry-enriched quantum critical spin chains, Phys. Rev. Lett. **129**, 210601 (2022).

[49] D. E. Parker, T. Scaffidi, and R. Vasseur, Topological Luttinger liquids from decorated domain walls, Phys. Rev. B **97**, 165114 (2018).

[50] R. Verresen, Topology and edge states survive quantum criticality between topological insulators, arXiv:2003.05453.

[51] X.-J. Yu, S. Yang, H.-Q. Lin, and S.-K. Jian, Universal entanglement spectrum in one-dimensional gapless symmetry protected topological states, Phys. Rev. Lett. **133**, 026601 (2024).

[52] H.-L. Zhang, H.-Z. Li, S. Yang, and X.-J. Yu, Quantum phase transition and critical behavior between the gapless topological phases, Phys. Rev. A **109**, 062226 (2024).

[53] Y. Hidaka, S. C. Furuya, A. Ueda, and Y. Tada, Gapless symmetry-protected topological phase of quantum antiferromagnets on anisotropic triangular strip, Phys. Rev. B **106**, 144436 (2022).

[54] L. Su and M. Zeng, Gapless symmetry-protected topological phases and generalized deconfined critical points from gauging a finite subgroup, Phys. Rev. B **109**, 245108 (2024).

[55] R. Wen and A. C. Potter, Bulk-boundary correspondence for intrinsically gapless symmetry-protected topological phases from group cohomology, Phys. Rev. B **107**, 245127 (2023).

[56] C. M. Duque, H.-Y. Hu, Y.-Z. You, V. Khemani, R. Verresen, and R. Vasseur, Topological and symmetry-enriched random quantum critical points, Phys. Rev. B **103**, L100207 (2021).

[57] T. Ando, Gauging on the lattice and gapped/gapless topological phases, arXiv:2402.03566.

[58] S. Prembabu, R. Thorngren, and R. Verresen, Boundary-deconfined quantum criticality at transitions between symmetry-protected topological chains, Phys. Rev. B **109**, L201112 (2024).

[59] U. Borla, R. Verresen, J. Shah, and S. Moroz, Gauging the Kitaev chain, SciPost Phys. **10**, 148 (2021).

[60] S.-J. Huang and M. Cheng, Topological holography, quantum criticality, and boundary states, arXiv:2310.16878.

[61] S.-C. Chang and P. Hosur, Absence of Friedel oscillations in the entanglement entropy profile of one-dimensional intrinsically gapless topological phases, arXiv:2201.07260.

[62] X.-J. Yu and W.-L. Li, Fidelity susceptibility at the Lifshitz transition between the noninteracting topologically distinct quantum critical points, Phys. Rev. B **110**, 045119 (2024).

[63] R. Wen and A. C. Potter, Classification of 1+1D gapless symmetry protected phases via topological holography, arXiv:2311.00050.

[64] T. Scaffidi, D. E. Parker, and R. Vasseur, Gapless symmetry-protected topological order, Phys. Rev. X **7**, 041048 (2017).

[65] R. Thorngren, A. Vishwanath, and R. Verresen, Intrinsically gapless topological phases, Phys. Rev. B **104**, 075132 (2021).

[66] L. Li, M. Oshikawa, and Y. Zheng, Decorated defect construction of gapless-SPT states, SciPost Phys. **17**, 013 (2024).

[67] L. Li, M. Oshikawa, and Y. Zheng, Intrinsically/purely gapless-SPT from non-invertible duality transformations, arXiv:2307.04788.

[68] N. Tantivasadakarn, R. Thorngren, A. Vishwanath, and R. Verresen, Pivot Hamiltonians as generators of symmetry and entanglement, SciPost Phys. **14**, 012 (2023).

[69] N. Tantivasadakarn, R. Thorngren, A. Vishwanath, and R. Verresen, Building models of topological quantum criticality from pivot Hamiltonians, SciPost Phys. **14**, 013 (2023).

[70] R. Verresen, N. G. Jones, and F. Pollmann, Topology and edge modes in quantum critical chains, Phys. Rev. Lett. **120**, 057001 (2018).

[71] N. G. Jones and R. Verresen, Asymptotic correlations in gapped and critical topological phases of 1D quantum systems, J. Stat. Phys. **175**, 1164 (2019).

[72] W. Choi, M. Knap, and F. Pollmann, Finite temperature entanglement negativity of fermionic symmetry protected topological phases and quantum critical points in one dimension, arXiv:2310.20566.

[73] R. R. Kumar, N. Roy, Y. R. Kartik, S. Rahul, and S. Sarkar, Signatures of topological phase transition on a quantum critical line, Phys. Rev. B **107**, 205114 (2023).

[74] R. R. Kumar, Y. Kartik, S. Rahul, and S. Sarkar, Multi-critical topological transition at quantum criticality, Sci. Rep. **11**, 1004 (2021).

[75] M. Jangjan and M. V. Hosseini, Floquet engineering of topological metal states and hybridization of edge states with bulk states in dimerized two-leg ladders, Sci. Rep. **10**, 14256 (2020).

[76] M. Jangjan and M. V. Hosseini, Topological phase transition between a normal insulator and a topological metal state in a quasi-one-dimensional system, Sci. Rep. **11**, 12966 (2021).

[77] M. Jangjan and M. V. Hosseini, Topological properties of subsystem-symmetry-protected edge states in an extended quasi-one-dimensional dimerized lattice, Phys. Rev. B **106**, 205111 (2022).

[78] M. Jangjan, L. E. F. Foa Torres, and M. V. Hosseini, Floquet topological phase transitions in a periodically quenched dimer, Phys. Rev. B **106**, 224306 (2022).

[79] A. Dutta and A. Dutta, Probing the role of long-range interactions in the dynamics of a long-range Kitaev chain, Phys. Rev. B **96**, 125113 (2017).

[80] M. Van Regemortel, D. Sels, and M. Wouters, Information propagation and equilibration in long-range Kitaev chains, Phys. Rev. A **93**, 032311 (2016).

[81] G. Francica and L. Dell'Anna, Correlations, long-range entanglement, and dynamics in long-range Kitaev chains, Phys. Rev. B **106**, 155126 (2022).

[82] S. B. Jäger, L. Dell'Anna, and G. Morigi, Edge states of the long-range Kitaev chain: An analytical study, Phys. Rev. B **102**, 035152 (2020).

[83] S. Mondal, S. Bandyopadhyay, S. Bhattacharjee, and A. Dutta, Detecting topological phase transitions through entanglement between disconnected partitions in a Kitaev chain with long-range interactions, Phys. Rev. B **105**, 085106 (2022).

[84] A. Alecce and L. Dell'Anna, Extended Kitaev chain with longer-range hopping and pairing, Phys. Rev. B **95**, 195160 (2017).

[85] F. Ares, J. G. Esteve, F. Falceto, and A. R. de Queiroz, Entanglement entropy in the long-range Kitaev chain, Phys. Rev. A **97**, 062301 (2018).

[86] J. Fraxanet, U. Bhattacharya, T. Grass, D. Rakshit, M. Lewenstein, and A. Dauphin, Topological properties of the long-range Kitaev chain with Aubry-André-Harper modulation, Phys. Rev. Res. **3**, 013148 (2021).

[87] Z.-X. Gong, M. F. Maghrebi, A. Hu, M. L. Wall, M. Foss-Feig, and A. V. Gorshkov, Topological phases with long-range interactions, Phys. Rev. B **93**, 041102(R) (2016).

[88] K. Patrick, T. Neupert, and J. K. Pachos, Topological quantum liquids with long-range couplings, Phys. Rev. Lett. **118**, 267002 (2017).

[89] Y. R. Kartik, R. R. Kumar, S. Rahul, N. Roy, and S. Sarkar, Topological quantum phase transitions and criticality in a longer-range Kitaev chain, Phys. Rev. B **104**, 075113 (2021).

[90] Z. Gong, T. Guaita, and J. I. Cirac, Long-range free fermions: Lieb-robinson bound, clustering properties, and topological phases, Phys. Rev. Lett. **130**, 070401 (2023).

[91] N. G. Jones, R. Thorngren, and R. Verresen, Bulk-boundary correspondence and singularity-filling in long-range free-fermion chains, Phys. Rev. Lett. **130**, 246601 (2023).

[92] O. Viyuela, L. Fu, and M. A. Martin-Delgado, Chiral topological superconductors enhanced by long-range interactions, Phys. Rev. Lett. **120**, 017001 (2018).

[93] W. Son, L. Amico, R. Fazio, A. Hamma, S. Pascazio, and V. Vedral, Quantum phase transition between cluster and antiferromagnetic states, Europhys. Lett. **95**, 50001 (2011).

[94] P. Smacchia, L. Amico, P. Facchi, R. Fazio, G. Florio, S. Pascazio, and V. Vedral, Statistical mechanics of the cluster Ising model, Phys. Rev. A **84**, 022304 (2011).

[95] Z.-X. Guo, X.-J. Yu, X.-D. Hu, and Z. Li, Emergent phase transitions in a cluster Ising model with dissipation, Phys. Rev. A **105**, 053311 (2022).

[96] R. Verresen, R. Moessner, and F. Pollmann, One-dimensional symmetry protected topological phases and their transitions, Phys. Rev. B **96**, 165124 (2017).

[97] G. Zhang and Z. Song, Topological characterization of extended quantum Ising models, Phys. Rev. Lett. **115**, 177204 (2015).

[98] S.-J. Gu, Fidelity approach to quantum phase transitions, Int. J. Mod. Phys. B **24**, 4371 (2010).

[99] S.-J. Gu and H.-Q. Lin, Scaling dimension of fidelity susceptibility in quantum phase transitions, Europhys. Lett. **87**, 10003 (2009).

[100] A. W. Sandvik, Computational studies of quantum spin systems, in *Lectures on the Physics of Strongly Correlated Systems XIV: Fourteenth Training Course in the Physics of Strongly Correlated Systems*, AIP Conf. Proc. No. 1297 (AIP, Melville, NY, 2010), pp. 135–338.

[101] D. Schwandt, F. Alet, and S. Capponi, Quantum Monte Carlo simulations of fidelity at magnetic quantum phase transitions, Phys. Rev. Lett. **103**, 170501 (2009).

[102] A. F. Albuquerque, F. Alet, C. Sire, and S. Capponi, Quantum critical scaling of fidelity susceptibility, Phys. Rev. B **81**, 064418 (2010).

[103] E. J. König, A. Levchenko, and N. Sedlmayr, Universal fidelity near quantum and topological phase transitions in finite one-dimensional systems, Phys. Rev. B **93**, 235160 (2016).

[104] H.-L. Zhang, J.-H. Lü, K. Chen, X.-J. Yu, F. Wu, Z.-B. Yang, and S.-B. Zheng, Critical quantum geometric tensors of parametrically-driven nonlinear resonators, Opt. Express **32**, 22566 (2024).

[105] X.-J. Yu, Dynamical phase transition and scaling in the chiral clock Potts chain, Phys. Rev. A **108**, 062215 (2023).

[106] P. Francesco, P. Mathieu, and D. Sénéchal, *Conformal Field Theory* (Springer, Berlin, 2012).

[107] P. Ginsparg, Applied conformal field theory, arXiv:hep-th/9108028.

[108] J. W. Britton, B. C. Sawyer, A. C. Keith, C.-C. J. Wang, J. K. Freericks, H. Uys, M. J. Biercuk, and J. J. Bollinger, Engineered two-dimensional Ising interactions in a trapped-ion quantum simulator with hundreds of spins, Nature (London) **484**, 489 (2012).

[109] K. Zhang, P. Wang, and Z. Song, Majorana flat band edge modes of topological gapless phase in 2D Kitaev square lattice, Sci. Rep. **9**, 4978 (2019).

[110] J. S. Douglas, H. Habibian, C.-L. Hung, A. V. Gorshkov, H. J. Kimble, and D. E. Chang, Quantum many-body models with cold atoms coupled to photonic crystals, Nat. Photonics **9**, 326 (2015).

[111] F. Pientka, L. I. Glazman, and F. von Oppen, Topological superconducting phase in helical Shiba chains, Phys. Rev. B **88**, 155420 (2013).

[112] G. H. Low and I. L. Chuang, Hamiltonian simulation by qubitization, Quantum **3**, 163 (2019).

[113] Z. Tao, T. Yan, W. Liu, J. Niu, Y. Zhou, L. Zhang, H. Jia, W. Chen, S. Liu, Y. Chen, and D. Yu, Simulation of a topological phase transition in a Kitaev chain with long-range coupling using a superconducting circuit, Phys. Rev. B **101**, 035109 (2020).

[114] R. Barends *et al.*, Digital quantum simulation of fermionic models with a superconducting circuit, Nat. Commun. **6**, 7654 (2015).